JOURNAL OF APPLIED CRYSTALLOGRAPHY

ISSN: 1600-5767
journals.iucr.org/j

High-temperature X-ray scattering studies of atomic layer deposited IrO_2

Mikko J. Heikkilä, Jani Hämäläinen, Esa Puukilainen, Markku Leskelä and Mikko Ritala

J. Appl. Cryst. (2020). **53**, 369–380

JOURNAL OF APPLIED CRYSTALLOGRAPHY

ISSN 1600-5767

Received 3 May 2019
Accepted 26 January 2020

Edited by D. Pandey, Indian Institute of Technology (Banaras Hindu University), Varanasi, India

‡ Current affiliation: Picosun Oy, Masalantie 365, Masala 02430, Finland.
§ Current affiliation: Vauhti Speed Oy, Pamilonkatu 9, Joensuu 80100, Finland.

Keywords: IrO_2; atomic layer deposition; ALD; high-temperature X-ray diffraction; HTXRD; high-temperature X-ray reflectivity; HTXRR.

Supporting information: this article has supporting information at journals.iucr.org/j

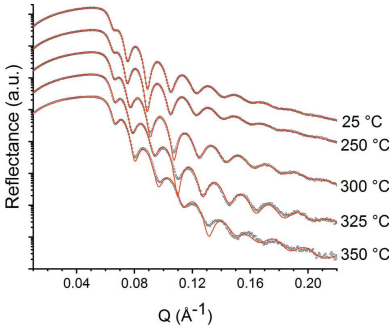

High-temperature X-ray scattering studies of atomic layer deposited IrO_2

Mikko J. Heikkilä,* Jani Hämäläinen,‡ Esa Puukilainen,§ Markku Leskelä and Mikko Ritala

Department of Chemistry, University of Helsinki, PO Box 55 (A. I. Virtasen aukio 1), University of Helsinki 00014, Finland. *Correspondence e-mail: mikko.j.heikkila@helsinki.fi

IrO_2 is an important material in numerous applications ranging from catalysis to the microelectronics industry, but despite this its behaviour upon annealing under different conditions has not yet been thoroughly studied. This work provides a detailed investigation of the annealing of IrO_2 thin films using *in situ* high-temperature X-ray diffraction and X-ray reflectivity (HTXRR) measurements from room temperature up to 1000°C in oxygen, nitrogen, forming gas and vacuum. Complementary *ex situ* scanning electron microscopy and atomic force microscopy measurements were conducted. The combined data show the dependencies of crystalline properties and surface morphology on the annealing temperature and atmosphere. The reduction of IrO_2 to Ir takes place at a temperature as low as 150°C in forming gas, but in oxygen IrO_2 is stable up to 800°C and evaporates as a volatile oxide at higher temperatures. The IrO_2 crystallite size remains constant in oxygen up to 400°C and increases above that, while in the more reducing atmospheres the Ir crystallites grow continuously above the phase-change temperature. The role of HTXRR in the analysis is shown to be important since its high sensitivity allows one to observe changes taking place in the film at temperatures much below the phase change.

1. Introduction

Iridium oxide has found use in a surprisingly wide variety of applications, despite the cost and rarity of the raw material. The earliest studies of IrO_2 were conducted by Claus as early as 1860 (Claus, 1860) and further by Wöhler and Witzmann in 1908 (Wöhler & Witzmann, 1908), but broader interest towards the material arose in the mid-1960s when dimensionally stable anodes were introduced for the chlor-alkali industry (Hackwood *et al.*, 1982; Trasatti, 2000). New applications were found in the 1980s when electrochromism and applicability for water electrolysis were discovered (Hackwood *et al.*, 1982). Today, the field of possible applications has diversified even further, ranging from the still ongoing electrochromic studies (Wen *et al.*, 2014) and water electrolysis (Rasten *et al.*, 2003; Yagi *et al.*, 2005; Hou *et al.*, 2006; Carmo *et al.*, 2013; Bernicke *et al.*, 2015; Abbott *et al.*, 2016; da Silva *et al.*, 2017) to unitized regenerative fuel cells (Pettersson *et al.*, 2006; Antolini, 2014), pH sensors (Huang *et al.*, 2011) and biosensors (Shim *et al.*, 2012), and, in medicine, cardiovascular stents (O'Brien & Carroll, 2009) and neural stimulation and detection (Cogan, 2008).

Many of the aforementioned applications utilize IrO_2 as particles or as thick and very rough films. The field that probably places the largest demands on high-quality thin films is microelectronics. IrO_2 has been explored most often as the top (Park *et al.*, 2005) or bottom electrode, *e.g.* in ferroelectric

memories, multiferroics or microelectromechanical systems devices (Lee *et al.*, 1999; Pinnow *et al.*, 2001, 2002; Gong *et al.*, 2013; Tomczyk *et al.*, 2017; Potrepka *et al.*, 2017; Okuyama, 2016), since it works as a diffusion barrier, has good phase stability at high temperatures under oxidizing conditions and is lattice matching with many ferroelectric materials, showing good structural and chemical compatibility. IrO_2 is also very conducting, its bulk resistivity being 35–60 μΩ cm. Furthermore, it has superior fatigue properties (Okuyama, 2016; Tomczyk *et al.*, 2017) and even radiation hardness (Brewer *et al.*, 2016) over commonly used Pt electrodes.

IrO_2 has been synthesized using a wide selection of methods. Thermal decomposition has been widely used (Jang & Rajeshwar, 1987; Hou *et al.*, 2006), as has reactive sputtering (Hackwood *et al.*, 1982; Sanjinés *et al.*, 1989; Lee *et al.*, 1999; Pinnow *et al.*, 2001, 2002; Cogan, 2008; Kim, Kwon, Kwak & Kang, 2008). Anodization of an Ir film (Cogan, 2008) and thermal oxidation of metallic iridium (Bayer & Wiedemann, 1975; Chalamala *et al.*, 1999, 2000) have been in use for a long period of time. Furthermore, IrO_2 thin films are also deposited hydrothermally (da Silva *et al.*, 2017) using the Adams fusion method (Rasten *et al.*, 2003; Abbott *et al.*, 2016), spray pyrolysis (Patil *et al.*, 2003), electro-deposition (Yagi *et al.*, 2005), sol–gel methods (Bernicke *et al.*, 2015), pulsed-laser deposition (Gong *et al.*, 2009; Hou *et al.*, 2017), laser ablation (Wang *et al.*, 2006; Gong *et al.*, 2013), chemical vapour deposition (CVD) (Liao *et al.*, 2001; Jürgensen *et al.*, 2017) and atomic layer deposition (ALD) (Hämäläinen *et al.*, 2008, 2014). Among the various thin-film deposition methods, ALD offers unsurpassed conformality and thickness uniformity properties, making it the method of choice for coating highly complex shapes (Ritala & Niinistö, 2009; George, 2010; Leskelä *et al.*, 2014).

Although the stability and microstructure of IrO_2 are important *e.g.* in catalytic and oxygen evolution/reduction applications, they are also critical in microelectronics and integration into thin-film devices. While many methods have been used to deposit IrO_2, there are surprisingly few detailed studies of how IrO_2 behaves during post-deposition annealing. The most often used method for analysis is X-ray diffraction (XRD) (Jang & Rajeshwar, 1987; Pinnow *et al.*, 2001, 2002; Sanjinés *et al.*, 1989; Kim, Shim *et al.*, 2008; Bayer & Wiedemann, 1975; Chalamala *et al.*, 1999, 2000; Gong *et al.*, 2009; Chen *et al.*, 1997). Pinnow *et al.* (2001, 2002) even used XRD for stress analysis of an IrO_2 film as a function of temperature. Thermogravimetry was used in some early studies (Hackwood *et al.*, 1982; Jang & Rajeshwar, 1987; Bayer & Wiedemann, 1975), as was calorimetry (Jang & Rajeshwar, 1987). Liao *et al.* (1997) used Raman spectroscopy, X-ray photoelectron spectroscopy (XPS) was used in a couple of studies (Sanjinés *et al.*, 1989; Peuckert, 1984), and gases evolved during annealing have been analysed a few times (Hackwood *et al.*, 1982; Pinnow *et al.*, 2002; Chalamala *et al.*, 2000). A change in film resistivity during annealing was studied by Sanjinés *et al.* (1989). While detailed experiments on thermal behaviour were conducted as early as the 1980s, the films were often at least partially hydrated.

The aim of the present study was to perform a detailed high-temperature X-ray scattering study on atomic layer deposited IrO_2 thin films that were annealed in different atmospheres: O_2, N_2, forming gas (5% H_2 in N_2) and vacuum. The changes in unit-cell parameters as determined by high-temperature X-ray diffraction (HTXRD) are presented, as well as information on the atmosphere-dependant decomposition into Ir. Changes in film roughness and surface morphology were followed using high-temperature X-ray reflectivity (HTXRR), atomic force microscopy (AFM) and field emission scanning electron microscopy (FESEM). The phase-change behaviour is discussed and the benefits of HTXRR in detecting changes in the film before actual phase changes occur are emphasized.

2. Experimental

Iridium oxide thin films were deposited from $Ir(acac)_3$ (acac = acetylacetonate) and ozone at 185°C in a hot-wall flow-type F-120 ALD reactor using a process developed by Hämäläinen *et al.* (2008). The reactor was operated under a nitrogen pressure of about 10 mbar (1 bar = 100 000 Pa). Nitrogen (99.9995%) was produced with a NITROX UHPN 3000 nitrogen generator and used as a carrier and purging gas. Silicon (100) was used as a substrate. Before loading into the reactor, the substrates were rinsed with ethanol and blown dry with nitrogen to remove dust particles. $Ir(acac)_3$ (99.9%, ABCR) was sublimed from an open boat held inside the reactor at 155°C. Ozone was produced with a Wedeco Ozomatic Modular 4 HC ozone generator from oxygen (99.999%, Linde Gas) and pulsed into the reactor through a needle valve and a solenoid valve from the main ozone flow line. The estimated ozone concentration output of the generator was about 100 g $N^{-1}m^{-3}$. A total of 1000 ALD cycles were applied in the process, where the pulse and purge times for both precursors were 1 s each, producing films with a thickness of 340 Å.

Film crystallinity and phase structure were determined with a PANalytical X'Pert Pro MPD diffractometer using Cu $K\alpha$ radiation. High-temperature measurements were conducted in an Anton Paar HTK1200N oven. Oxygen (99.9999%), nitrogen (99.999%, further purified with Entegris 35KF-I-4R inert gas purifier) and forming gas (5% H_2 in N_2) were used at 10–50 mbar above ambient pressure (due to the check valve at the furnace outlet) for annealing in gaseous atmospheres, while vacuum measurements were conducted at $<10^{-3}$ mbar. The temperature was raised at a rate of 15°C min^{-1} and a 2 min waiting period preceded each 30 min measurement done at constant temperature, giving an effective heating rate of approximately 1.2 C min^{-1}. Grazing-incidence X-ray diffraction (GIXRD) measurements were done using a multilayer mirror, a 0.18° parallel-plate collimator and a PIXcel detector. The angle of incidence was 1° for all GIXRD measurements. The same setup with an additional 0.1 mm parallel-plate collimator slit was used for the HTXRR measurements. Before the X-ray reflectivity (XRR) measurements, the correct sample height position and omega offset were determined for each temperature. The *MAUD* software package

was used for Rietveld refinement of the diffractograms (Lutterotti *et al.*, 2004). Fitting to the XRR data was done using *REFLEX35* (Vignaud & Gibaud, 2019) and *MOTOFIT* (Nelson, 2006), and on a few occasions *STOCHFIT* was used to evaluate the structure (Danauskas *et al.*, 2008).

The XRR fitting procedure consisted of several steps. The whole film thickness was first modelled with ten slices of variable density, and in each slice the roughness was limited to one half of the thickness. The layers were thinner closer to the interface (in order to detect better any abrupt changes taking place there) and at the surface (in case the Nevot–Croce roughness model was not adequate for modelling the surface roughness, which might not be Gaussian due to the changes taking place while annealing). Importantly, the effect of the sample size and incident-beam size were taken into account in *REFLEX35*, as the sample length was below 18 mm due to the furnace size.

The XRR data of the as-deposited layers were fitted using as free parameters the surface-layer thickness and roughness, the buffer SiO_2 layer thickness and roughness, and all the densities. All the other values were kept constant. The data were first fitted using a genetic algorithm in *MOTOFIT* or Nelder–Mead minimization in *REFLEX35*, in order to approach the global minimum of the fit. After both methods gave close-to-equal results, the fit was improved in *REFLEX35* using the interior-point algorithm (Vignaud & Gibaud, 2019) to reach the absolute local minimum. The densities are scattering length densities (SLDs) and thus not dependent on the stoichiometry of the film. After a satisfactory fit had been reached, the same values were used as starting values for the next temperature data set, unless there were large differences, in which case global optimizations were again tried at first.

The film morphology was studied with a Hitachi S-4800 field emission scanning electron microscope. For AFM studies a Veeco Instruments Multimode V with Nanoscope V controller was used. Samples were measured in tapping mode in air using a phosphorus-doped silicon probe (RTESP) supplied by Veeco Instruments. Several scans were performed on different parts of the samples to check the uniformity of the surface. Final images were taken from a scanning area of 2×2 µm with a scanning frequency of 0.5 Hz, and no image processing except flattening was performed. Roughness values k were calculated as root-mean-square values (R_q).

3. Results and discussion

3.1. X-ray scattering

3.1.1. Annealing in an oxygen atmosphere. Rietveld refinement of the GIXRD data of the as-deposited film is depicted in Fig. 1(*a*). No other phases than tetragonal IrO_2 are present (Bolzan *et al.*, 1997). Since the widths of the first two reflections in the IrO_2 diffractograms were very different [FWHM = 1.37° 2θ for the (110) reflection at 28.0° 2θ, and 0.65° 2θ for the (101) reflection at 34.9° 2θ], the crystallite size and shape were considered to be anisotropic and refinements were thus made using the Popa rules for anisotropic crystallite size (Popa, 1998). Similar XRD patterns were obtained by Abbott *et al.* (2016) in their powder synthesis and, on the basis of high-resolution transmission electron microscopy, this was related to preferred crystallite growth in the [001] and [112] directions. Since the intensity ratios differed from the standard ratios and because no real texture information was available, an arbitrary texture model was used to correct the intensity differences. The same methodology was used to refine the results acquired in nitrogen, vacuum and forming gas. The R_{wp} values remain quite high (almost 0.15 at worst) in all refinements due to high noise related to the fast acquisition. However, this was considered acceptable for the level of detail studied here.

GIXRD measurements of an IrO_2 film heated in oxygen are depicted in Fig. 1(*b*). The tetragonal IrO_2 phase remains up to 800°C, and above that temperature IrO_2 is barely observed in the diffractograms. No new phases appear upon the disappearance of IrO_2. The broad bump observed at higher temperatures around 55° 2θ originates from the Si substrate.

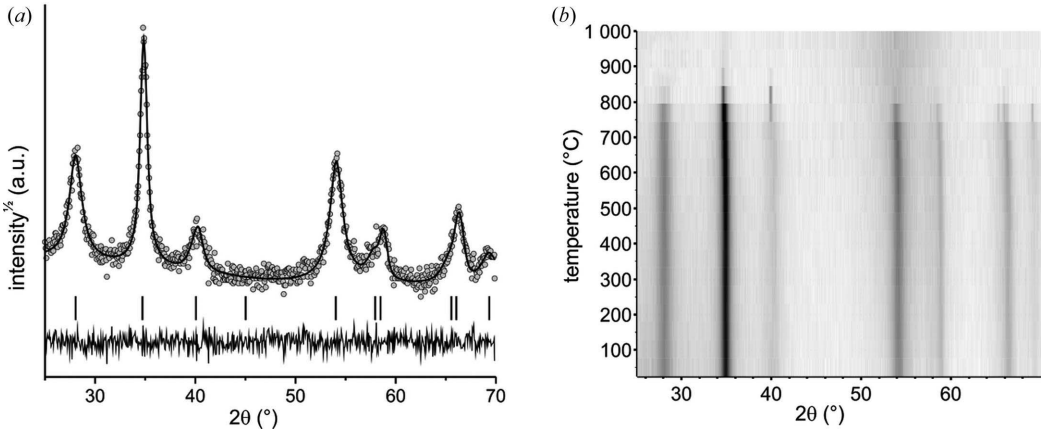

Figure 1
(*a*) Rietveld refinement of the GIXRD data of the as-deposited IrO_2 film. The grey circles represent the measured data and the solid line the simulation. Vertical bars show the locations of the reflections in the reference data, and the difference between the measured and simulated data is shown at the bottom. (*b*) High-temperature GIXRD data of an IrO_2 film annealed in an oxygen atmosphere.

Our results are well in line with several other studies performed in either oxygen or air, where IrO_2 has been observed to be stable up to 750–850°C (Lee *et al.*, 1999; Chen *et al.*, 1997; Cha & Lee, 1999; Zhang *et al.*, 2005; Kim, Kwon, Jeong *et al.*, 2008; Gong *et al.*, 2009; Pinnow *et al.*, 2002). Similarly to our case, Chalamala *et al.* (1999, 2000) noted that, after heating their pulsed-laser-deposited films to 900°C, there was no sign of Ir on the surface according to XPS, and similar findings of IrO_2 nanowires being vaporized have been reported by Zhang *et al.* (2005). This is in contrast to the fact that bulk IrO_2 should be stable up to 1100°C before decomposing (Rumble, 2018). Some authors suggest that the disappearance of the film is due to the formation of volatile IrO_x species (Chalamala *et al.*, 1999; Kim, Kwon, Jeong *et al.*, 2008), and Shim *et al.* (2012) even used this to grow IrO_2 films by evaporating IrO_2 at 1000°C and condensing the vapours onto the substrate at 700°C.

In contrast to the findings above, IrO_2 has been observed to decompose to Ir at high temperatures – one group observed this at 850°C (Kim, Kwon, Jeong *et al.*, 2008) and another at 1000–1050°C (Jang & Rajeshwar, 1987). According to Sanjinés *et al.* (1989), sputter-deposited iridium oxide decomposes already at 400°C, although this was probably a decomposition of a hydrated film into either Ir or IrO_2, depending on the degree of hydration of the sample. This indicates that the decomposition of IrO_2 has a dependence on temperature and the partial pressure of oxygen during annealing, as explained by Cha & Lee (1999) and discussed later in Section 3.1.3.

The unit-cell parameters were determined using Rietveld refinement and are depicted in Fig. 2. Horizontal arrows point to the literature values reported by Bolzan *et al.* (1997). While the *a* axis is quite close to the literature value of 4.5051 Å, the *c* axis is slightly shorter (3.1584 Å in the literature). The unit-cell parameters remain nearly constant up to 500°C with a tiny maximum for the *c* axis at 200–250°C. Above 500°C, the unit-cell parameters increase until the data are no longer refinable above 750°C. This is quite different from the literature data shown in Fig. 2, where the averages of two powder sample measurement results by Rao & Iyengar (1969) and Bayer & Wiedemann (1975) are plotted as dotted (*a* axis) and dashed (*c* axis) lines. The room-temperature values are already different, and the slopes are different as well. This indicates that thermal expansion is restricted, probably due to the different thermal expansion coefficients between the silicon substrate and the IrO_2 film. The faster expansion of the cell parameters above 600°C could be related to stress relaxation and recrystallization, as similar results were observed by Pinnow *et al.* (2001, 2002) with their sputtered films.

In addition to the HTXRD studies, XRR was measured as a function of temperature, and the results are shown in Fig. 3. As explained in the *Experimental* section, initial fits to these data were performed using a ten-slice model, but ultimately a two-layer model was enough to fit the data accurately (see Fig. S1 in the supporting information). A thin (16 Å) layer with an SLD of 9.0×10^{-5} Å^{-2} was found next to the substrate, and this is thought to be a layer composed of IrO_2 with a small amount of Ir, as the SLD value for bulk IrO_2 is smaller, about 7.8×10^{-5} Å^{-2}. The SLD of the rest of the film was 7.6×10^{-5} Å^{-2}, close to the bulk value. A small amount of Ir at the interface is plausible when considering the original process paper by Hämäläinen *et al.* (2008). There, the Ir/O ratio was constant at 1:2 when the deposition was done at 185°C, while at a deposition temperature of 200°C the ratio was almost 1:1 at the substrate interface, suggesting partial reduction to metallic Ir at the beginning of the growth. Even though our film was deposited at 185°C where the stoichiometry should be 1:2, a layer of Ir a few nanometres thick at the interface would have been practically invisible to XRD or to

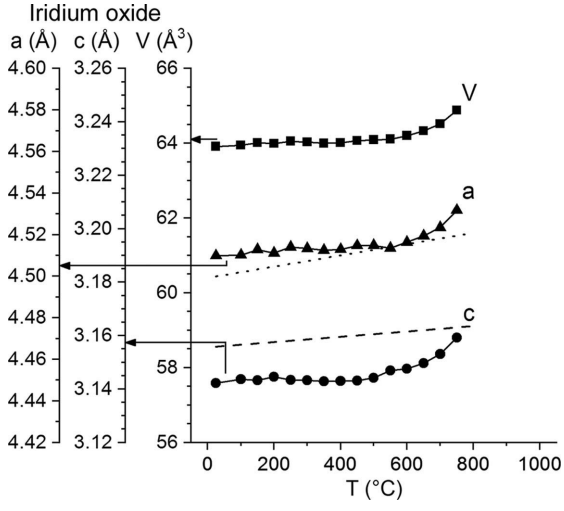

Figure 2
Rietveld-refined unit-cell parameters as a function of temperature for an IrO_2 film annealed in oxygen. The three *y* axes on the left-hand side are for the *a* axis, *c* axis and volume of the IrO_2 unit cell. The horizontal arrows point to the axes at the positions of the literature values of the room-temperature unit-cell dimensions. The averages of literature values are shown as a dotted line for the *a* axis and a dashed line for the *c* axis. (Rao & Iyengar, 1969; Bayer & Wiedemann, 1975).

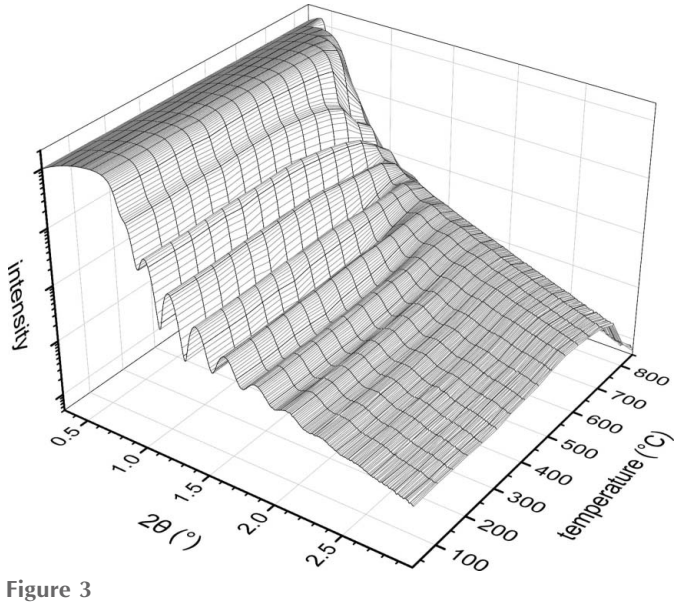

Figure 3
HTXRR measurements of an IrO_2 film in an oxygen atmosphere.

compositional analysis with elastic recoil detection analysis and might have been present in their study as well.

The acquired SLD, total thickness and surface roughness values are depicted as a function of temperature in Fig. 4(*a*)

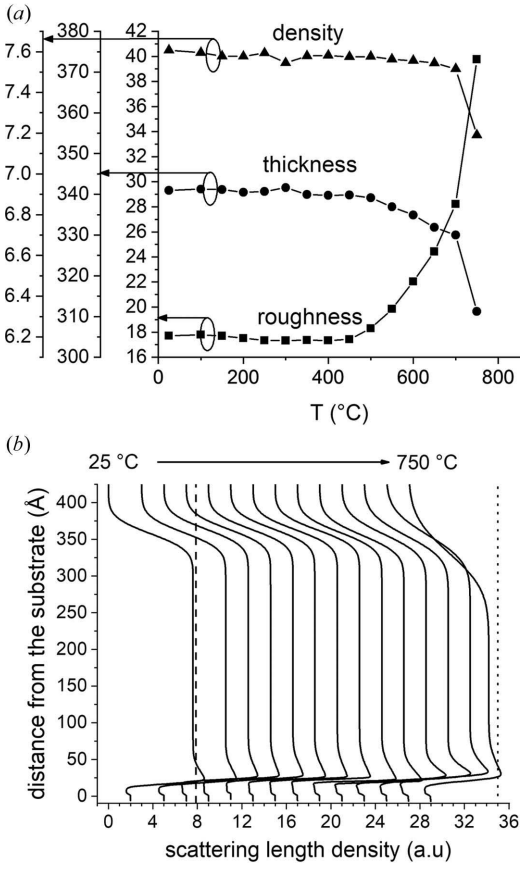

Figure 4
(*a*) IrO_2 SLD ($\times 10^{-5}$ Å^{-2}), total thickness (Å) and surface roughness (Å) of the oxygen-annealed film as a function of temperature. (*b*) SLD as a function of distance from the substrate at varying temperature. The curves are shifted horizontally for clarity by two SLD units for each 50°C. The two vertical lines represent the SLDs of bulk IrO_2 for the measurements conducted at 25°C (dashed) and 750°C (dotted).

(fits to the data are shown in Fig. S1 in the supporting information). All the values remain quite constant up to 450°C, and this is also seen in the shape of the SLD plot in Fig. 4(*b*). At 450°C the higher-density layer at the interface gets thinner and denser, probably due to coalescence of the remaining Ir. Although a pure Ir film starts to oxidize at 500°C according to our earlier study (Heikkilä *et al.*, 2011), the diffusion-barrier properties of the deposited IrO_2 seem to prohibit the Ir layer from oxidizing completely, even at higher temperatures.

At 500°C and higher temperatures the roughness begins to increase rapidly, most likely due to the crystal growth of the film as shown later in Section 3.1.5. As this temperature coincides with the onset of the increase in unit-cell parameters, the structure probably relaxes at that point. Even though macrostress was not found on the basis of the Rietveld refinement, the average microstrain decreases towards higher temperatures (see Section 3.1.5). The overall change in density is a combination of several effects, as the increase in unit-cell size should lead to a density decrease while the grain growth reduces the number of grain boundaries and thus densifies the film. Indeed, from 25°C to 700°C the values of bulk IrO_2 film SLD and unit-cell volume both change about 1% in opposite directions, while simultaneously the total layer thickness decreases by 11 Å (about 4%), the densification of the Ir layer alone being 4 Å (see Fig. S2 in the supporting information). It appears that the film gets thinner more than the density change would suggest, but the reason for this is unknown.

Above 650°C, the density and thickness both decrease, most likely due to the onset of film decomposition as observed in diffraction data at higher temperatures, but also as crack formation in 750°C scanning electron microscopy images (see Section 3.1.6).

3.1.2. Annealing in a nitrogen atmosphere. High-temperature XRD results for an IrO_2 film heated in a nitrogen atmosphere are depicted in Fig. 5. When the temperature reaches ~650°C, IrO_2 begins to decompose to metallic iridium, and this transformation is completed at 750°C. Ir then remains stable up to the highest studied temperature of 1000°C.

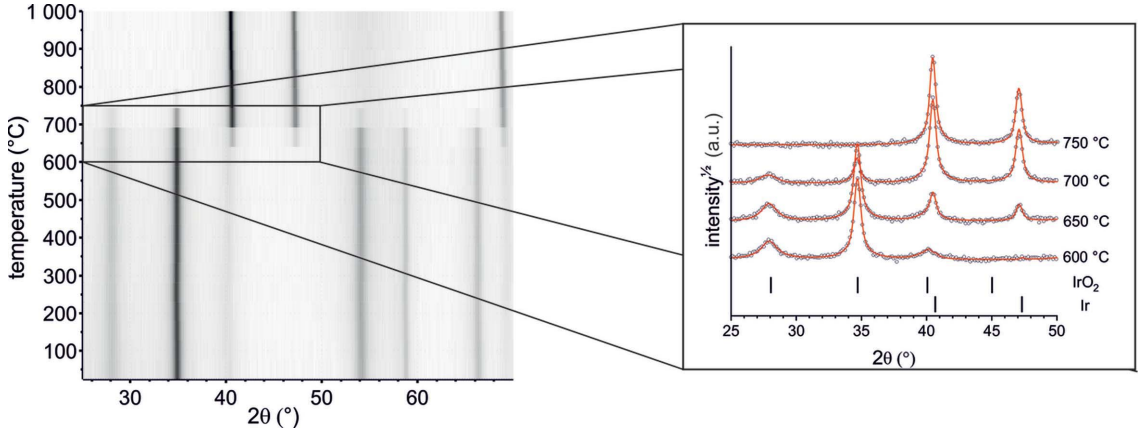

Figure 5
GIXRD measurements of an IrO_2 film annealed in a nitrogen atmosphere. The enlarged region on the right-hand side depicts the diffractograms at temperatures where decomposition takes place; open circles are the measured data and red lines the Rietveld fits to the data.

Our results agree well with the earlier studies. IrO_2 films made by Kim, Shim *et al.* (2008) decomposed to Ir between 500–750°C in argon, while Chen *et al.* (1997) noticed partial decomposition from IrO_2 to Ir taking place at 700°C with their sputtered films. Zhang *et al.* (2005) observed their IrO_2 nanowires starting to decompose to Ir at 700°C and no IrO_2 was left at 800°C. Slightly different results were obtained by Hackwood *et al.* (1982), who found their IrO_2 films to be stable at 790°C in Ar. Sanjinés *et al.* (1989) observed a noticeable change in film resistivity below 300°C when the film was heated in Ar, and the resistivity change was completed at 500°C, but this was probably due to a gradual decomposition from hydrated IrO_2, first to IrO_2 and then to Ir. In the work by Choi *et al.* (2007), IrO_2 nanodots embedded in an SiO_2 film were found to be stable at 800°C, which may be important when considering bottom electrode application where IrO_2 is often covered by oxide layers.

The unit-cell parameters as a function of temperature are depicted in Fig. 6. While the parameters remained quite constant in oxygen (Fig. 2), in nitrogen there is a slight increase in the parameters up to 250°C that is much more obvious than during the O_2 annealing. The reason for this is unclear, but as Sanjinés *et al.* (1989) observed a resistivity drop within a similar temperature range due to a partial loss of oxygen, this might also be the case here. On the other hand, this temperature range is just above the deposition temperature and might be additionally related to film relaxation. Above 250°C there is a small decrease in the unit-cell parameters, after which they stay constant until the decomposition into Ir takes place. On heating further, Ir shows a close-to-linear thermal expansion behaviour.

The effect of the heating rate was tested by measuring a constant 2° 2θ window during heating (see Fig. S3 in the supporting information). One measurement took 1 min, and the heating rate was either 20 or 1°C min^{-1}. At the higher heating rate the phase transformation seemed to occur at a temperature 25°C higher than with the slower heating. However, as the temperature increased by 20°C during each fast scan, there was also a rather large error in the temperature with the higher heating rate.

Fitting the XRD data was much more complicated than when the annealing was done in oxygen. Selected XRR curves, SLD profiles, thickness and surface roughness are depicted in Fig. 7 (all the fits are shown in Fig. S1 of the supporting information). There is practically no change between room temperature and the measurement done at 250°C, but the

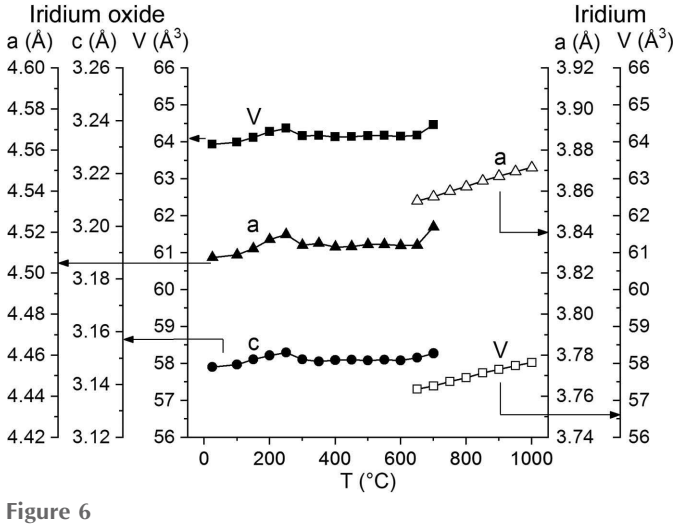

Figure 6
Rietveld-refined unit-cell parameters as a function of temperature for an IrO_2 film annealed in nitrogen. The three *y* axes on the left-hand side are for the *a* axis, *c* axis and volume of the IrO_2 unit cell, and the two *y* axes on the right-hand side are for the *a* axis and volume of the Ir unit cell. The horizontal arrows point to the axes at the positions of the literature values of the room-temperature unit-cell dimensions.

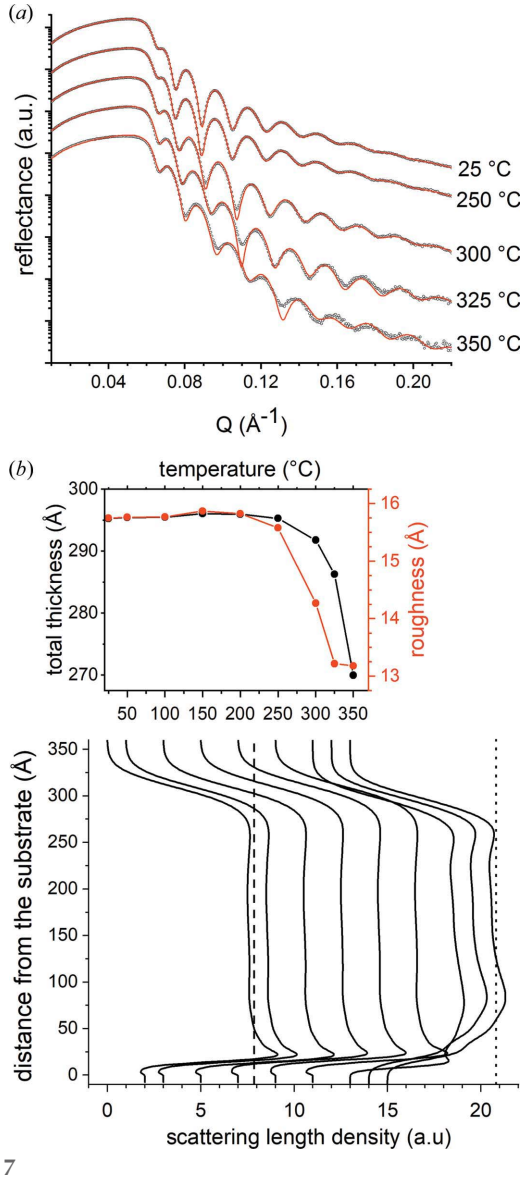

Figure 7
(*a*) Selected XRR curves and fits for the samples annealed in nitrogen. The curves are shifted vertically for clarity. (*b*) The upper plot shows the total thickness (Å) and the surface roughness (Å) of the annealed film as a function of temperature. SLD curves at the same temperatures are shown in the lower plot. The curves are shifted horizontally for clarity by two SLD units for each 50°C. The two vertical lines represent the SLDs of bulk IrO_2 for the measurements conducted at 25°C (dashed) and 750°C (dotted).

reflectogram clearly changes at 300°C and even more so at higher temperatures. The fringe separation increase is obviously caused by the thickness of the film decreasing from 295 to 270 Å between 250 and 350°C, as shown in the upper panel of Fig. 7(*b*). The decay rate of the amplitude envelope is usually directly related to the increase in surface roughness, which implies that here the surface roughness decreases when the sample is heated above 300°C, and according to the fit it decreases from 15.7 to 13.2 Å [see Fig. 7(*b*)]. However, density gradients at the interfaces and within the film itself may cause changes in the amplitude as well. In this case it appears that there are large variations in the density, as the best fit to the 300°C data was obtained when there was a decrease in density close to the substrate interface, the native oxide was removed from the model and the Si substrate roughness was allowed to increase, as seen in the SLD plot of Fig. 7(*b*). The reason for this is not clear and would require more *ex situ* measurements like cross-section transmission electron microscopy. This trend continued up to 350°C, while above that temperature the data could not be fitted with any reasonable model. Fig. 7(*b*) also shows the bulk IrO_2 SLD value as a dotted line for the sample measured at 350°C, and it is quite clear that the main part of the film is still IrO_2, as observed in the HTXRD experiment (Fig. 5).

As part of the SLD curve reaches higher levels than the IrO_2 bulk value, it is plausible that IrO_2 already starts to reduce partially at this stage, even though there is no indication of this in the XRD. Since the SLD is still far below the bulk value for Ir (14.5×10^{-5} Å^{-2}), there are probably small Ir crystallites embedded in the IrO_2 matrix, making it impossible to see them with XRD here. The partial reduction probably causes the thickness decrease as well.

There are multiple effects affecting the density. The release of oxygen will decrease the SLD of the material (even though the number of electrons is low compared with Ir), while at the same time thermal expansion will decrease the density as well. In addition, when IrO_2 starts to reduce to Ir, there are locally higher-SLD Ir parts, but the reduction may also produce voids or shrinkage in the film, again lowering the density. One should keep in mind that composing the model film from multiple slices of varying density has some drawbacks, since several different SLD profiles might give the same reflectivity curve because the phase information is lost in XRR measurements (van der Lee, 2000). However, it has been used successfully on many occasions (Sun *et al.*, 2006; Danauskas *et al.*, 2008; Mishra *et al.*, 2012), and here several different solutions were evaluated until the chosen model gave the best fit while still being physically reasonable.

Interestingly, the temperature range of the first change in the reflectivity curves coincides with the small change found in the lattice parameters (Fig. 6) in the same temperature range, so some form of reconstruction of the film/substrate interface is probably taking place. Since the same was not observed in the HTXRR data from the O_2-annealed sample, it is probably not related to stress relief or similar reasons but may relate to a possible loss of oxygen that would cause density differences within the film. Note that all the changes take place much below the phase-change temperature and do not seem to be related to changes in crystallinity (see Section 3.1.5). This emphasizes the efficiency of HTXRR in detecting minor changes in thin films during annealing, and similar results were also obtained in our earlier study related to the oxidation of noble metals (Heikkilä *et al.*, 2011).

3.1.3. Annealing in a vacuum. Stability in a vacuum and at low oxygen partial pressures is important, especially when IrO_2 is used as a bottom electrode, as the following layer is often deposited under such conditions. GIXRD measurements of an IrO_2 film during annealing in a vacuum are shown in Fig. 8. The transformation to the Ir phase begins at 200°C, much lower than was observed when annealing in a nitrogen atmosphere. IrO_2 decomposition is complete at 250°C. Poorly crystalline Ir forms first and larger crystallites start to grow above 500°C.

Peuckert (1984) observed an oxidized Ir surface to decompose into elements in UHV at temperatures between 577 and 627°C, and he noted that this was much higher than the temperature of 227°C observed with bulk IrO_2. Sanjinés *et al.* (1989) found a significant decrease in resistivity around 200°C, which is close to the temperature where we observed the phase change here. According to XPS studies, the O/Ir ratio

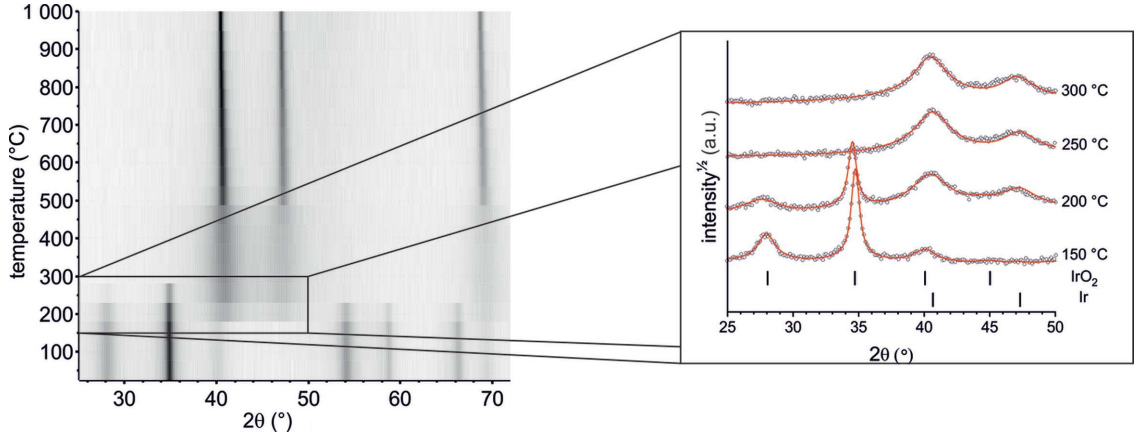

Figure 8
GIXRD measurements of an IrO_2 film annealed in a vacuum. The enlarged region on the right-hand side depicts the diffractograms at temperatures where the decomposition takes place; open circles are the measured data and red lines the Rietveld fits to the data.

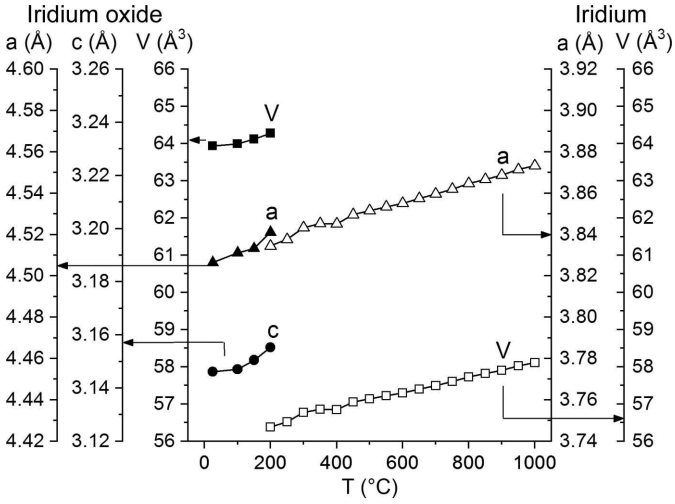

Figure 9
Rietveld-refined unit-cell parameters as a function of temperature for an IrO_2 film annealed in a vacuum. The three *y* axes on the left-hand side are for the *a* axis, *c* axis and volume of the IrO_2 unit cell, and the two *y* axes on the right-hand side are for the *a* axis and volume of the Ir unit cell. The horizontal arrows point to the axes at the positions of the literature values of the room-temperature unit-cell dimensions.

was 0.7 between 200 and 400°C, and thus a mixture of IrO_2 clusters in Ir metal was thought to be present. Above 400°C the film was all metal with no oxygen detected. In their very interesting paper related to the deoxidation of a sputtered IrO_2 film, Cha & Lee (1999) used thermodynamics to calculate the relationship between the O_2 partial pressure and temperature required for the IrO_2 dissociation. According to their results, under the conditions of our experiments ($<10^{-3}$ mbar) the dissociation temperature would be 400–500°C, much higher than what we and some others have observed. Gong *et al.* (2013) have complemented the study of Cha and Lee, and they reported that their pulsed-laser-deposited IrO_2 films were stable at a temperature as high as 800°C when the O_2 partial pressure was 100 mbar, but the stability limit decreased to 300°C at a lower O_2 partial pressure of 10^{-8} mbar. They noticed that the deposition method has an effect on the film stability but did not comment on the effect of film thickness, which will most likely affect the stability as well. They used 500 nm films in their study, while here the thickness is more than an order of magnitude lower, which might explain changes occurring at lower temperatures. Byun & Lee (2004) conducted a similar experiment by annealing a 50 nm metal-oxide CVD IrO_2 film in a vacuum with different O_2 partial pressures. Their results show that the O_2 partial pressure needed to keep the films as IrO_2 was several orders of magnitude higher than in the study by Gong *et al.* (2013), which means that for the same partial pressure the films would decompose at a lower temperature and the film thickness may indeed be an important parameter. Possible reasons for this are that there is less material to decompose, shorter diffusion lengths are needed for the oxygen to be removed, and the less developed crystallinity includes more defects through which the reduction can begin.

The refined unit-cell parameters are depicted in Fig. 9. When compared with the annealing in nitrogen, the increase in the unit-cell parameters is clearly faster up to decomposition at 200°C. When the film was annealed in nitrogen, there was an increase in the unit-cell parameters up to 250°C, but the unit-cell parameters stabilized after that. The reason for this could be that, in the nitrogen atmosphere, the released oxygen is not immediately removed from the surface as in the vacuum case, but reacts with iridium, so there might be some kind of an equilibrium for a while, allowing IrO_2 to partially reconstruct instead of fully decomposing. With thin layers one also has to take into account the possible oxidizing impurities in the N_2 stream, even though the already pure N_2 (99.999%) was further purified before entering the furnace.

3.1.4. Annealing in forming gas. GIXRD measurements during the annealing of an IrO_2 film in an atmosphere of forming gas (5% H_2 in N_2) are shown in Fig. 10 and the refined unit-cell parameters in Fig. 11. The unit cell expands much faster before decomposition compared with annealing done in either a vacuum or nitrogen, indicating a highly unstable state. Decomposition to Ir occurs at 150°C, which is 50°C lower than observed in a vacuum. Literature references on annealing in a

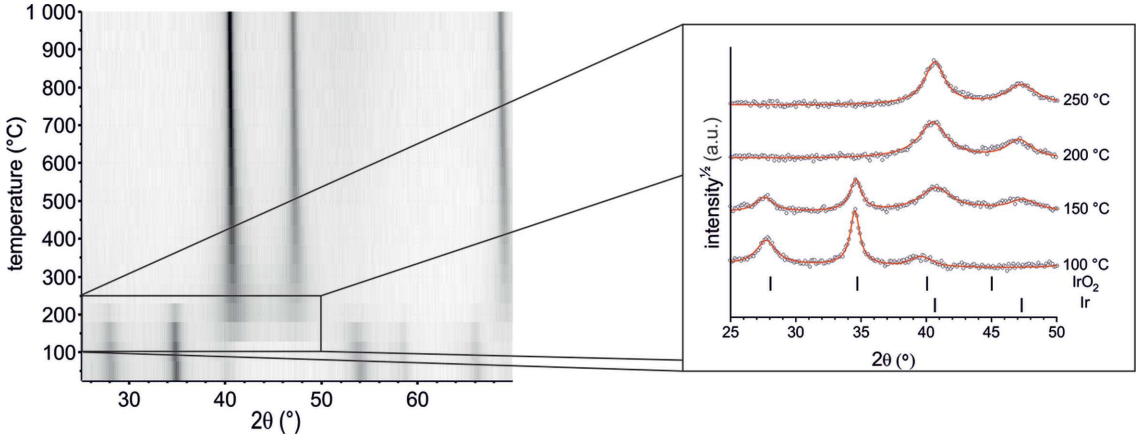

Figure 10
GIXRD measurements of an IrO_2 film annealed in forming gas. The enlarged region on the right-hand side depicts the diffractograms at temperatures where the decomposition takes place; open circles are the measured data and red lines the Rietveld fits to the data.

reducing atmosphere are rare. Chen *et al.* (1997) noticed that their sputtered IrO_2 film reduced completely to Ir and peeled off at 450°C, but they did not report results at other temperatures. Cross *et al.* (2002) studied the behaviour of IrO_2 top electrodes by annealing IrO_2/PZT/Pt/Si films (PZT is lead zirconium titanate) in 3% D_2/N_2 or 3% H_2/N_2 atmospheres at 6.0 mbar and found that, according to secondary ion mass spectroscopy, oxygen loss from the IrO_2 film surface has already started after 10 min at 200°C and progresses more deeply when heated for a longer time. Auger electron spectroscopy was used to confirm that, after 15 min, the film surface was reduced to metallic Ir and voids appeared on the surface. Metallic Ir was thought to be catalytically active in dissociating deuterium into D^+ ions which then diffused into the PZT.

3.1.5. Effect of annealing on crystallite size. The refined crystallite sizes in different atmospheres as a function of temperature are depicted in Fig. 12. On the basis of the results from the annealing in oxygen, the crystallites are elongated in the [001] direction and smaller in the [100] and [010] directions, suggesting cylindrical or ellipsoidal shapes. Similar crystallite size anisotropy was observed in the samples annealed in other atmospheres but, for the sake of clarity, only average values are plotted in Fig. 12(*b*). For the sample annealed in a nitrogen atmosphere, the crystallite size trend is similar to that of the oxygen-annealed sample up to 650°C where the decomposition takes place. Above that temperature there is a strong increase in the Ir crystallite size. Interestingly, the IrO_2 sample annealed in a vacuum breaks into tiny Ir crystallites after decomposition at 200°C, with a subsequent slow increase in the crystallite size up to 700°C. Above that temperature the crystallite size increases at a rate close to that observed for the nitrogen-annealed sample. Since the trend in unit-cell parameters and crystallite sizes above 650°C is similar for both nitrogen- and vacuum-annealed samples, the Ir atoms seem to be quite mobile to diffuse along the surface to form larger crystallites, and this is also observed in the FESEM images (Fig. 13). In the forming gas IrO_2 breaks into small Ir crystallites at an even lower temperature than in a vacuum, but unlike in N_2 or vacuum, the crystallite size of Ir increases above the decomposition temperature quite linearly.

Even though no macrostrain could be found, microstrain was analysed together with the crystallite size, and average values for the samples annealed in O_2 and N_2 are shown in Fig. 12(*c*). There seems to be a decreasing trend in both atmospheres until the onset of crystallite size increase. The onset temperature for the IrO_2 crystallite size growth is around 400°C, a slightly lower temperature than where the change in unit-cell parameters was observed (Fig. 2) or the surface roughness began to increase (Fig. 4). Although directly

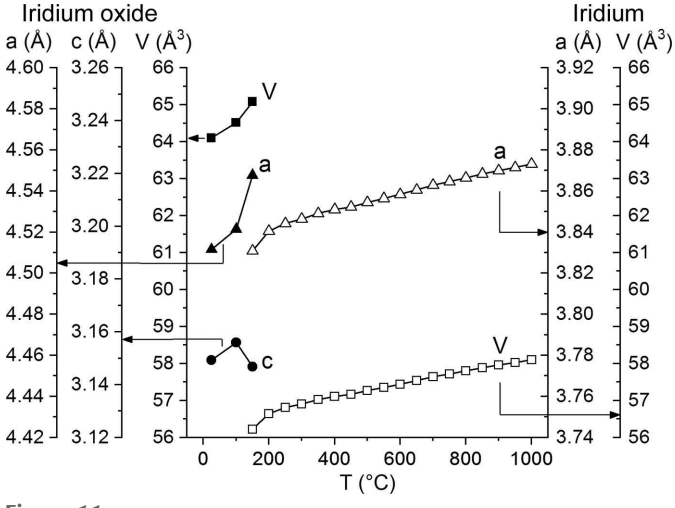

Figure 11
Rietveld-refined unit-cell parameters as a function of temperature for an IrO_2 film annealed in forming gas. The three *y* axes on the left-hand side are for the *a* axis, *c* axis and volume of the IrO_2 unit cell, and the two *y* axes on the right-hand side are for the *a* axis and volume of the Ir unit cell. The horizontal arrows point to the axes at the positions of the literature values of the room-temperature unit-cell dimensions.

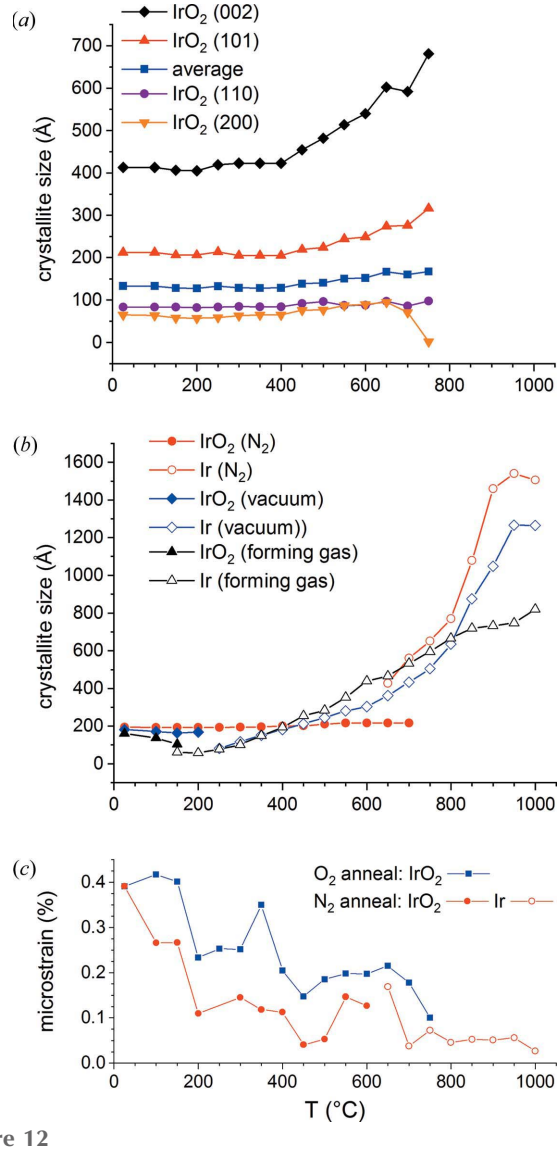

Figure 12
(*a*) The average crystallite size and the size calculated for different lattice planes as a function of annealing temperature in oxygen. (*b*) The average crystallite sizes in nitrogen, vacuum and forming gas. (*c*) The average microstrain of the IrO_2 film annealed in O_2 and in N_2.

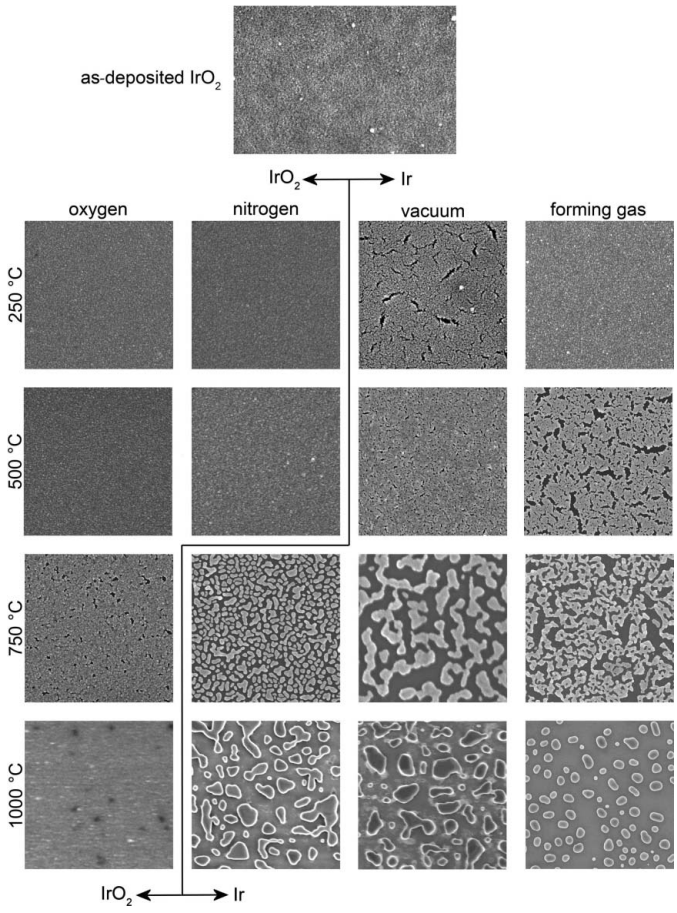

Figure 13
FESEM images of the IrO_2 films heated to different temperatures in different atmospheres. The image sizes are 3 × 2 μm for the as-deposited film and 2 × 2 μm for the others.

comparable crystallite size growth data are not available, Hackwood *et al.* (1982) noticed that a sputtered amorphous IrO_2 film crystallized at around 300°C, and similar observations were reported for hydrothermal IrO_x by da Silva *et al.* (2017) between 300 and 400°C and for mesoporous IrO_2 by Ortel *et al.* (2011) at 450°C, although in the latter case the first signs of crystallization were observed at 300°C by transmission electron microscopy selected-area electron diffraction. In addition, Bernicke *et al.* (2015) noticed initial signs of sintering at 550°C in their porous films. All these data agree quite well with our crystallite growth temperature range.

3.1.6. Surface characterization. For surface characterization, the films were heated inside the Anton Paar oven in different atmospheres to selected temperatures and then cooled to room temperature. The temperatures were selected on the basis of the HTXRD measurements and similar heating rates were used. FESEM images of the annealed films are shown in Fig. 13. The film annealed in oxygen looks unchanged up to 500°C, while the film annealed at 750°C is much rougher. These results agree well with the XRD (Fig. 2) and XRR (Fig. 4) results, since there is only a slight change in the crystallite size or in the film density, thickness and roughness up to 500°C, while at higher temperatures the crystallite size and film roughness increase strongly. The r.m.s.

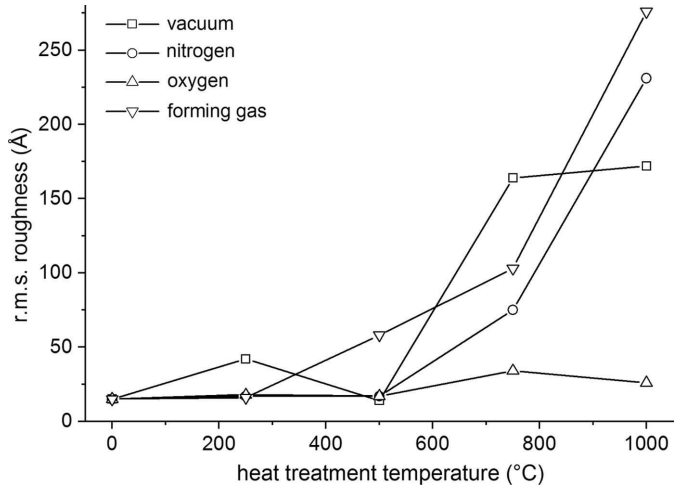

Figure 14
The r.m.s. roughnesses of the IrO_2 films heated to different temperatures in different atmospheres as acquired from the AFM images.

roughness obtained by AFM is also consistent with the XRR and FESEM results, as seen in Fig. 14. For the film annealed at 1000°C in oxygen, both FESEM and AFM indicate that there is basically nothing left of IrO_2 on the surface, which is reasonable since there was no diffraction signal at that temperature either.

On the basis of the HTXRD results, the nitrogen-annealed films should look comparable to the oxygen-annealed films up to 500°C, and this is also evident from the FESEM images and AFM data. At 750°C there is only the Ir phase left in the nitrogen sample (Fig. 5), and this is observed as island formation in the FESEM and AFM images. At 1000°C the islands continue to grow. In a vacuum, the film begins to crack at 250°C, which is consistent with the diffraction data (Fig. 8), and this may be the reason for the bump in the 250°C AFM data as well (Fig. 14). There is no island formation, though, and the film surface is also quite smooth at 500°C. This agrees well with the small crystallite size of the vacuum-annealed film [Fig. 12(*b*)]. The formation of an island network is observed at 750°C and separate islands at 1000°C. In contrast to the nitrogen-annealed film, the island size seems to remain the same and there is only a small change in the r.m.s. roughness.

4. Conclusions

High-temperature X-ray diffraction and X-ray reflectivity measurements in oxygen, nitrogen, vacuum and forming gas were conducted on atomic layer deposited IrO_2, and the surface morphology was further investigated using scanning electron microscopy and atomic force microscopy. Detailed analysis of the unit-cell parameters, phase composition and crystallinity was performed and the results were compared with the literature. The results of the present study give valuable information for researchers and industry by deepening the knowledge of the temperature and atmosphere stability of IrO_2 films and the development of their microstructure upon annealing under different conditions.

It was shown that in oxygen the IrO_2 film is stable up to 800°C, and at higher temperatures it evaporates as a volatile oxide. The stability was evident from the HTXRR data as well, since all the parameters remained essentially constant up to 500°C, above which the film densified and the roughness started to increase until the destruction of the layer above 750°C. The cause of the increasing roughness is clear from the crystallite sizes, which remain constant up to 400°C and then start to increase.

When annealed in forming gas, vacuum or nitrogen, IrO_2 decomposed to Ir at 150, 200 or 650°C, respectively. The crystallite sizes of the resulting Ir films increased continuously above the reduction temperature while the film turned first into a network of islands and then, with increasing temperature, into separate islands. HTXRR was not well suited to studying the annealing in forming gas or vacuum due to the abrupt changes in the films at low temperatures. However, HTXRR gave useful information about the annealing in nitrogen as it showed how the film structure changed and developed density variations within the film even though there was no phase change or change in crystallinity. This sensitivity makes HTXRR a very attractive technique to observe even the smallest changes in thin films during annealing. It should be noted that in many thin-film device stacks the internal structure might be more important than the actual phase-change temperature. The behaviour of the interfaces during annealing is much better understood with *in situ* studies as they give more information about the development of film structure than numerous *ex situ* measurements.

References

Abbott, D. F., Lebedev, D., Waltar, K., Povia, M., Nachtegaal, M., Fabbri, E., Copéret, C. & Schmidt, T. J. (2016). *Chem. Mater.* **28**, 6591–6604.

Antolini, E. (2014). *ACS Catal.* **4**, 1426–1440.

Bayer, G. & Wiedemann, H. G. (1975). *Thermochim. Acta*, **11**, 79–88.

Bernicke, M., Ortel, E., Reier, T., Bergmann, A., Ferreira de Araujo, J., Strasser, P. & Kraehnert, R. (2015). *ChemSusChem*, **8**, 1908–1915.

Bolzan, A. A., Fong, C., Kennedy, B. J. & Howard, C. J. (1997). *Acta Cryst.* B**53**, 373–380.

Brewer, S. J., Deng, C. Z., Callaway, C. P., Paul, M. K., Fisher, K. J., Guerrier, J. E., Rudy, R. Q., Polcawich, R. G., Jones, J. L., Glaser, E. R., Cress, C. D. & Bassiri-Gharb, N. (2016). *J. Appl. Phys.* **120**, 024101.

Byun, K. & Lee, W.-J. (2004). *Jpn. J. Appl. Phys.* **43**, 2655–2660.

Carmo, M., Fritz, D. L., Mergel, J. & Stolten, D. (2013). *Int. J. Hydrogen Energy*, **38**, 4901–4934.

Cha, S. Y. & Lee, H. C. (1999). *Jpn. J. Appl. Phys.* **38**, L1128–L1130.

Chalamala, B. R., Wei, Y., Reuss, R. H., Aggarwal, S., Gnade, B. E., Ramesh, R., Bernhard, J. M., Sosa, E. D. & Golden, D. E. (1999). *Appl. Phys. Lett.* **74**, 1394–1396.

Chalamala, B. R., Wei, Y., Reuss, R. H., Aggarwal, S., Perusse, S. R., Gnade, B. E. & Ramesh, R. (2000). *J. Vac. Sci. Technol. B*, **18**, 1919–1922.

Chen, T.-S., Balu, V., Jiang, B., Kuah, S.-H., Lee, J. C., Chu, P., Jones, R. E., Zurcher, P., Taylor, D. J. & Gillespie, S. (1997). *Integr. Ferroelectr.* **16**, 191–198.

Choi, S., Cha, Y.-K., Seo, B.-S., Park, S., Park, J.-H., Shin, S., Seol, K. S., Park, J.-B., Jung, Y.-S., Park, Y., Park, Y., Yoo, I.-K. & Choi, S.-H. (2007). *J. Phys. D Appl. Phys.* **40**, 1426–1429.

Claus, C. (1860). *J. Prakt. Chem.* **80**, 282–317.

Cogan, S. F. (2008). *Annu. Rev. Biomed. Eng.* **10**, 275–309.

Cross, J. S., Horii, Y., Mizuta, N., Watanabe, S. & Eshita, T. (2002). *Jpn. J. Appl. Phys.* **41**, 698–701.

Danauskas, S. M., Li, D., Meron, M., Lin, B. & Lee, K. Y. C. (2008). *J. Appl. Cryst.* **41**, 1187–1193.

George, S. M. (2010). *Chem. Rev.* **110**, 111–131.

Gong, Y., Wang, C., Shen, Q. & Zhang, L. (2009). *Mater. Chem. Phys.* **116**, 573–577.

Gong, Y., Wang, C., Shen, Q. & Zhang, L. (2013). *Appl. Surf. Sci.* **285**, 324–330.

Hackwood, S., Dayem, A. H. & Beni, G. (1982). *Phys. Rev. B*, **26**, 471–478.

Hämäläinen, J., Kemell, M., Munnik, F., Kreissig, U., Ritala, M. & Leskelä, M. (2008). *Chem. Mater.* **20**, 2903–2907.

Hämäläinen, J., Ritala, M. & Leskelä, M. (2014). *Chem. Mater.* **26**, 786–801.

Heikkilä, M. J., Hämäläinen, J., Ritala, M. & Leskelä, M. (2011). *Z. Kristallogr. Proc.* **1**, 209–214.

Hou, X., Takahashi, R., Yamamoto, T. & Lippmaa, M. (2017). *J. Cryst. Growth*, **462**, 24–28.

Hou, Y.-Y., Hu, J.-M., Liu, L., Zhang, J.-Q. & Cao, C.-N. (2006). *Electrochim. Acta*, **51**, 6258–6267.

Huang, W.-D., Cao, H., Deb, S., Chiao, M. & Chiao, J. C. (2011). *Sens. Actuators A Phys.* **169**, 1–11.

Jang, G.-W. & Rajeshwar, K. (1987). *J. Electrochem. Soc.* **134**, 1830–1835.

Jürgensen, L., Frank, M., Pyeon, M., Czympiel, L. & Mathur, S. (2017). *Organometallics*, **36**, 2331–2337.

Kim, H. W., Shim, S. H., Myung, J. H. & Lee, C. (2008). *Vacuum*, **82**, 1400–1403.

Kim, S.-W., Kwon, S.-H., Jeong, S.-J., Park, J.-S. & Kang, S.-W. (2008). *Electrochem. Solid-State Lett.* **11**, H303–H305.

Kim, S.-W., Kwon, S.-H., Kwak, D.-K. & Kang, S.-W. (2008). *J. Appl. Phys.* **103**, 023517.

Lee, A. van der (2000). *Solid State Sci.* **2**, 257–278.

Lee, H.-S., Um, W.-S., Hwang, K.-T., Shin, H.-G., Kim, Y.-B. & Auh, K.-H. (1999). *J. Vac. Sci. Technol. A*, **17**, 2939–2943.

Leskelä, M., Niinistö, J. & Ritala, M. (2014). *Comprehensive Materials Processing*, edited by S. Hashmi, G. F. Batalha, C. J. van Tyne & B. Yilbas, Vol. 4, pp. 101–123. Amsterdam: Elsevier.

Liao, P. C., Chen, C. S., Ho, W. S., Huang, Y. S. & Tiong, K. K. (1997). *Thin Solid Films*, **301**, 7–11.

Liao, P. C., Huang, Y. S. & Tiong, K. K. (2001). *J. Alloys Compd.* **317–318**, 98–102.

Lutterotti, L., Chateigner, D., Ferrari, S. & Ricote, J. (2004). *Thin Solid Films*, **450**, 34–41.

Mishra, D., Benitez, M. J., Petracic, O., Badini Confalonieri, G. A., Szary, P., Brüssing, F., Theis-Bröhl, K., Devishvili, A., Vorobiev, A., Konovalov, O., Paulus, M., Sternemann, C., Toperverg, B. P. & Zabel, H. (2012). *Nanotechnology*, **23**, 055707.

Nelson, A. (2006). *J. Appl. Cryst.* **39**, 273–276.

O'Brien, B. & Carroll, W. (2009). *Acta Biomater.* **5**, 945–958.

Okuyama, M. (2016). *Features, Principles and Development of Ferroelectric Gate Field-Effect Transistors*, edited by B. Park, H. Ishiwara, M. Okuyama, S. Sakai & S. Yoon, pp. 3–20. Dordrecht: Springer Netherlands.

Ortel, E., Reier, T., Strasser, P. & Kraehnert, R. (2011). *Chem. Mater.* **23**, 3201–3209.

Park, T. J., Jeong, D. S., Hwang, C. S., Park, M. S. & Kang, N.-S. (2005). *Thin Solid Films*, **471**, 236–242.

Patil, P. S., Chigare, P. S., Sadale, S. B., Seth, T., Amalnerkar, D. P. & Kawar, R. K. (2003). *Mater. Chem. Phys.* **80**, 667–675.

Pettersson, J., Ramsey, B. & Harrison, D. (2006). *J. Power Sources*, **157**, 28–34.

Peuckert, M. (1984). *Surf. Sci.* **144**, 451–464.

Pinnow, C. U., Kasko, I., Dehm, C., Jobst, B., Seibt, M. & Geyer, U. (2001). *J. Vac. Sci. Technol. B*, **19**, 1857–1865.
Pinnow, C. U., Kasko, I., Nagel, N., Poppa, S., Mikolajick, T., Dehm, C., Hösler, W., Bleyl, F., Jahnel, F., Seibt, M., Geyer, U. & Samwer, K. (2002). *J. Appl. Phys.* **91**, 9591–9597.
Popa, N. C. (1998). *J. Appl. Cryst.* **31**, 176–180.
Potrepka, D. M., Rivas, M., Yu, H., Polcawich, R. G., Aindow, M. & Fox, G. R. (2017). *Thin Solid Films*, **638**, 127–137.
Rao, K. V. K. & Iyengar, L. (1969). *Curr. Sci.* **38**, 304–305.
Rasten, E., Hagen, G. & Tunold, R. (2003). *Electrochim. Acta*, **48**, 3945–3952.
Ritala, M. & Niinistö, J. (2009). *ECS Trans.* **25**(8), 641–652.
Rumble, J. R. (2018). Editor. *CRC Handbook of Chemistry and Physics*, Internet Version 2018, 99th ed., Section 4. Boca Raton: CRC Press/Taylor & Francis.
Sanjinés, R., Aruchamy, A. & Lévy, F. (1989). *J. Electrochem. Soc.* **136**, 1740–1743.
Shim, J. H., Lee, Y., Kang, M., Lee, J., Baik, J. M., Lee, Y., Lee, C. & Kim, M. H. (2012). *Anal. Chem.* **84**, 3827–3832.
Silva, G. C. da, Perini, N. & Ticianelli, E. A. (2017). *Appl. Catal. Environ.* **218**, 287–297.
Sun, Y., Frenkel, A. I., Isseroff, R., Shonbrun, C., Forman, M., Shin, K., Koga, T., White, H., Zhang, L., Zhu, Y., Rafailovich, M. H. & Sokolov, J. C. (2006). *Langmuir*, **22**, 807–816.
Tomczyk, M., Stroppa, D. G., Reaney, I. M. & Vilarinho, P. M. (2017). *Phys. Chem. Chem. Phys.* **19**, 14337–14344.
Trasatti, S. (2000). *Electrochim. Acta*, **45**, 2377–2385.
Vignaud, G. & Gibaud, A. (2019). *J. Appl. Cryst.* **52**, 201–213.
Wang, C., Gong, Y., Shen, Q. & Zhang, L. (2006). *Appl. Surf. Sci.* **253**, 2911–2914.
Wen, R.-T., Niklasson, G. A. & Granqvist, C. G. (2014). *Solar Energy Mater. Solar Cells*, **120**, 151–156.
Wöhler, L. & Witzmann, W. (1908). *Z. Anorg. Chem.* **57**, 323–352.
Yagi, M., Tomita, E. & Kuwabara, T. (2005). *J. Electroanal. Chem.* **579**, 83–88.
Zhang, F., Barrowcliff, R. & Hsu, S. T. (2005). *Proceedings of the 2005 International Conference on MEMS, Nano and Smart Systems*, pp. 418–420. IEEE Computer Society.